

A Fully-automatic Side-scan Sonar SLAM Framework

Jun Zhang, Yiping Xie, Li Ling and John Folkesson

Abstract—Side-scan sonar (SSS) is a lightweight acoustic sensor that is frequently deployed on autonomous underwater vehicles (AUV) to provide high-resolution seafloor image. However, using side-scan images to perform simultaneous localization and mapping (SLAM) remains a challenge due to lack of 3D bathymetric information and the lack of discriminant features in the sidescan images. To tackle this, we propose a feature-based SLAM framework using side-scan sonar, which is able to automatically detect and robustly match keypoints between paired side-scan images. We then use the detected correspondences as constraints to optimize the AUV pose trajectory. The proposed method is evaluated on real data collected by a Hugin AUV, using as a ground truth reference both manually-annotated keypoints and a 3D bathymetry mesh from multibeam echosounder (MBES). Experimental results demonstrate that our approach is able to reduce drifts compared to the dead-reckoning system. The framework is made publicly available for the benefit of the community*.

I. INTRODUCTION

Most commercial AUVs rely on the dead-reckoning system for underwater navigation, but this is subject to unbounded error due to accumulation of sensor uncertainties. The common solutions to limit such error are to use either global referencing system (i.e., GPS) that requires the vehicle to resurface regularly, or pre-installed acoustic ranging systems (e.g., long/urtrashort baseline), which are cumbersome to deploy and restrictive to limited range. An alternative solution is to incorporate sensor measurements of the environment to reduce the dead-reckoning drift using simultaneous localization and mapping (SLAM) method [1].

For AUV surveying deep undersea, the most frequently-used sensors are two types of sonars: side-scan sonar (SSS), useful for producing high resolution images of a large swath of the seafloor, and multibeam echosounder (MBES), useful for producing the 3D geometry of the seafloor albeit generally at a lower resolution than SSS. MBES uses beamforming to obtain directional information from the received sound waves and directly provides 3D data of the seabed as point clouds that are relatively easy to interpret for underwater SLAM applications [2] [3]. The main drawbacks of MBES, however, are their high cost, bulky size and high power consumption. SSS is more economical, lightweight and easier to deploy compared to MBES, well suited for small AUVs. It ensonifies the seafloor by emitting sound waves from the two sides (port and starboard) of the vehicle, and forms an image by stacking the pings along the vehicle’s travelling direction [4]. The high resolution, in principle, allows for

precise AUV localization, whilst the larger coverage allows for localization using large areas of the seafloor.

However, the problem of SLAM with SSS images is far from being solved, mainly due to the challenge of registering SSS images to one another and the lack of 3D information. In particular, raw SSS images are geometrically distorted and unevenly ensonified, making the appearance of same region of seabed vary in SSS images as observed from different positions. To address this, a canonical transformation is first applied to raw SSS images to reduce such distortions and redistribute the image pixels in equal size. Then a robust salient keypoint detection and matching algorithm, combining both geometric and appearance constraints, is proposed to find keypoint correspondences between overlapping images. The inability of measuring 3D data makes the estimate of AUV pose underdetermined, even with good associated keypoints.

In this paper, we propose a two-ping keypoint measurement model, which is formulated together with dead-reckoning constraints as a least-squares minimization problem, to solve for the relative pose between the two associated pings. All of such estimated poses serve as loop-closure constraints in a pose graph and global optimization then refines the whole AUV pose trajectory. The ping-based solution is chosen instead of the commonly-used, computational efficient submap-based methods [5] [6] (that first group the pings into an image and then form a constraint between images based on assuming no dead-reckoning drift over the small scale of the image) due to having very sparse detected keypoints (see Fig. 3 left). Furthermore, we argue that our solution avoids the assumption that dead-reckoning drift can be neglected in a submap, while the computational cost is small due to the sparseness of the constraints.

We show how our proposed method performs using a variety of metrics on actual side-scan data. This includes evaluations used by hand annotating the images but in contrast to most previous works we show automatic detection of keypoints and only use the annotated keypoints for comparison. This demonstration of automatic detection is the main contribution while using annotated points and a mesh built from MBES data allows for some meaningful evaluations, something that are difficult with underwater data.

II. RELATED WORK

Research on SLAM with SSS has drawn considerable attention within the community in the past two decades. Among the earlier works, [7] [8] combine a stochastic map with Rauch-Tung-Striebel (RTS) filter to estimate AUV’s location, where the stochastic map is formulated as extended Kalman filter (EKF), with landmarks manually extracted

Jun Zhang, Yiping Xie, Li Ling and John Folkesson are with the KTH Royal Institute of Technology, 114 28 Stockholm, Sweden. {juzhang, yipingx, lililing, johnf}@kth.se

*The source code link will be provided here upon acceptance.

from the side-scan images. Later in [9], the authors propose to fuse acoustic ranging and side-scan sonar measurements in pose graph SLAM state estimation framework that avoids inconsistent solution caused by information lost during linearization [10], to achieve accurate AUV trajectory estimation. Similarly, [11] proves the capabilities of using SSS images in graph-based iSAM [12] algorithm to produce corrected sensor trajectories for image mosaicking. Issartel et al. [13] take a further step to incorporate switchable observation constraints in a pose graph to address false data association issue and guarantee robust solution. The above solutions prove the feasibility of using SSS information to help better localize AUVs, however, they rely on manual annotation of landmarks in SSS images, which goes against full autonomy in AUVs.

There are but few approaches attempting to concurrently address the problems of both SSS image association and SLAM. [5] proposes to use a boosted cascade of Haar-like features to perform automatic feature detection in SSS images. The correspondences are found by means of joint compatibility branch and bound (JCBB) algorithm [14], and used to update pose states in an EKF SLAM framework. By applying a similar framework, [15] combines local thresholds and template-based detectors with strict heuristics to avoid false associations. The integration of JCBB in EKF is arguably well-fitted to solve the complete SSS SLAM problem with fewer landmark measurements, but it suffers from inconsistent performance and offers lower accuracy when comparing to graph-based SLAM solution [16].

Lately, the fusing of visual and geometric information to accomplish data association becomes a trending solution. For instance, [17] uses elevation gradients as additional features to assist in associations between landmarks. In [18], the authors propose to construct features with 3D location and feature intensity, and associate between them through a modified version of iterative closest point (ICP) [19] scan matching method. In this paper, we follow the same idea and propose a robust keypoint detection and matching algorithm, which combines visual descriptors with geometric information from dead-reckoning data and sliding compatibility check to find keypoint correspondences between SSS images. The keypoints are fed into our graph-based SLAM framework to refine the dead-reckoning AUV trajectory.

Another line of work that is highly relevant is feature-based SLAM framework using forward looking sonars (FLS) [20] [21] [22]. The differences are mainly in the front-end due to different sensor modalities and the application scenarios. The typical range of FLS is from 1-2 meters to tens of meters, making it suitable for small-scale environment, while SSS for industrial-scale surveys are generally used to map seafloor of hundreds and thousands of meters in large-scale environment. FLS usually have a wide aperture, so that there is a large amount of overlapping between swaths from consecutive frames or when there is a loop closure. Solving such an acoustic bundle adjustment is very similar to using SSS with a submap-based approach but without the need to ignore the dead-reckoning errors within submaps.

III. METHODOLOGY

In this section, we describe the details of our proposed SSS SLAM framework, which takes pre-processed sonar image and dead-reckoning data as input, and outputs an optimized AUV pose trajectory. The proposed pipeline is summarized in Fig. 1, and it contains three main parts: image processing, data association and graph SLAM optimization.

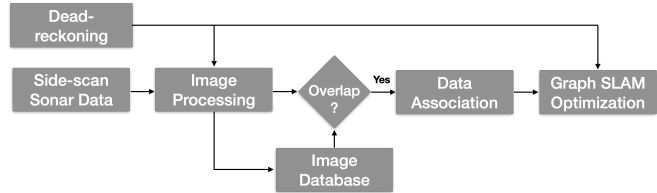


Fig. 1. Overview of our SSS SLAM framework.

A. Image Processing

1) *SSS Image Generation*: Raw side-scan sonar data is generated continuously ping by ping along the longitudinal direction, i.e., direction of travel. To obtain an informative representation of the seabed, the time series of return intensities from individual pings are layered to form side-scan images. In our work, given that the AUV follows a common lawnmower pattern with major overlap between swaths, the proposed framework takes the side-scan image formed by each swath as input. The raw SSS pings contain over $40k$ bins per ping. This high across-track resolution, together with the low along-track resolution ($\sim 0.5\text{m}$ per ping), significantly distorts the seabed appearance. To avoid this issue, the SSS pings are downsampled to 1301 bins per side (port and starboard).

2) *Canonical Transformation*: Data association across different SSS images is challenging, as the same physical area on the seabed will appear differently in the SSS images collected from different distances and angles. Furthermore, an SSS image will be distorted compared to an orthographic projection of the ensonified region and will vary in intensity as a function of the sonar position. To reduce such distortions, we apply a method [23] capable of transforming SSS images from different survey lines into a canonical representation, which includes two steps: intensity correction and sensor independent slant range correction. Intensity correction is performed to normalize the intensities across images based on the 'Lambertian' model [24] [25], with the SSS backscatter intensity being proportional to the cosine square [26] of the incidence angle. The slant range correction adjusts for the varying projection of side-scan pixels on the assumed horizontal seafloor. An adjustment of sine of the incidence angle is performed to be a distance along the horizontal, so that the pixels can be of fixed size in terms of slant range. More details can be found in [23].

3) *Geo-reference Image*: To approximately check whether any two of the SSS images are overlapped, we utilize the dead-reckoning data to make each pixel in SSS image geo-referenced [27], i.e., approximate the location of each pixel of an SSS image in the global reference coordinate. This

is also used to narrow the searching area when performing keypoint matching in data association. An example of our collected side-scan image after image processing is demonstrated in Fig. 2.

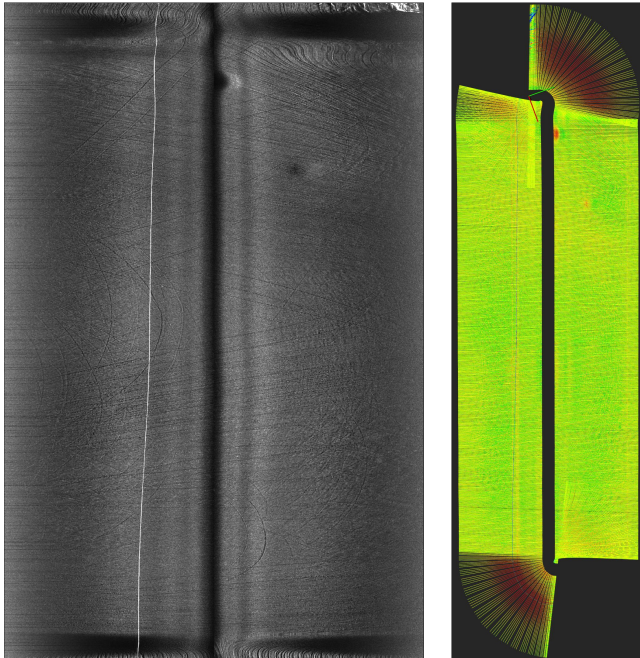


Fig. 2. Left: sample of our collected SSS images after processing, where trawling marks can be observed. Right: the corresponding geo-referenced image storing pixel positions relative to the AUV poses. Note that the color encodes pixel intensity that is best viewed in the left image.

B. Data Association

Once an overlapping area is found between a new SSS image and any image in the database, a data association process is performed to find feature correspondences between the overlapping images. In this work, salient keypoints are detected as sparse features and matched between images. Specifically, evenly distributed FAST [28] corners are detected in each SSS image by dividing each SSS image into grid cells and detecting corners in each cell. The reason for such a homogeneous distribution is to ensure good correspondences are found dispersedly, rather than locally in each SSS image, and thereby contribute to the optimization of most pings of the corresponding pose trajectory by adding them as constraints in the pose graph. Then SIFT [29] descriptor is extracted on the detected corners, which is discriminative and invariant to rotation and noise.

After feature extraction is done for a new SSS image (source), the detected keypoints are used to find their correspondences in the overlapping image (target) of the database. In this paper, a simple yet effective matching approach that combines both descriptor and geometric constraints is proposed, which consists of two parts: near neighbor search and a sliding compatibility check.

Near neighbor search uses the geo-referenced result of SSS images to find matching keypoints in local neighboring region, to avoid visual ambiguity in the case of brute-force

search. For each queried keypoint in the source image, we calculate the Euclidean distance between its geo-referenced coordinate and the ones of all keypoints in the target image. Keypoints within a radius threshold r are counted as matching candidates, where r is set empirically depending on the geometrical distance between two images. Then the matched keypoint is found among the candidates with minimum descriptor distance against the queried keypoint.

The sliding compatibility check is used to verify the consistency along rows (i.e., ping) direction of the found keypoint pairs. Ideally, all keypoint pairs detected in two overlapping SSS images should have the same row difference along parallel survey lines, if we had a constant AUV speed, direction, and ping rate. In this paper, a fast RanSaC [30] is performed by modelling the row difference as criteria, and then counting the consistency of all keypoint pairs as score to find the best inlier set. This allows eliminating many false matching pairs quickly. An example of detected keypoint correspondences is shown in Fig. 3 left.

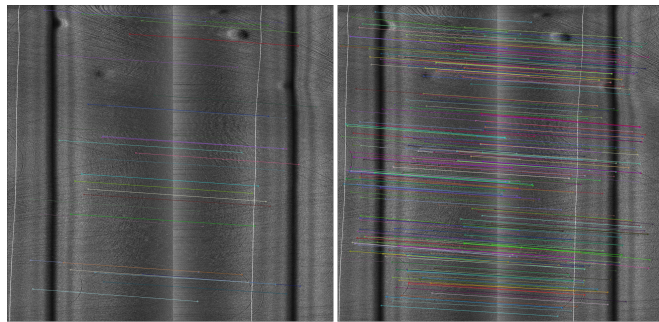


Fig. 3. Example of keypoint correspondences generated by our proposed algorithm (left) and manual annotations (right).

C. Graph SLAM Optimization

In this section, we show how each pair of the keypoint correspondences is used to construct a measurement model and solve for the relative pose between pings of the keypoint pair. The estimated relative pose and its uncertainty serve as loop-closure constraint to correct the drift of dead-reckoning in pose graph SLAM optimization.

1) *Keypoint Measurement Model*: We model the i^{th} measurement of a keypoint found in an image as a 2D measurement that constrains the slant range to the keypoint and that it lay in a plane perpendicular to the sonar array:

$$\mathbf{z}_i = \begin{pmatrix} r_i \\ 0 \end{pmatrix} = \hat{\mathbf{z}}_i + \boldsymbol{\eta} = \begin{pmatrix} \sqrt{\pi(\mathbf{o}\mathbf{x}) \cdot \pi(\mathbf{o}\mathbf{x})} \\ (1, 0, 0) \cdot \pi(\mathbf{o}\mathbf{x}) \end{pmatrix} + \boldsymbol{\eta}, \quad (1)$$

where $\boldsymbol{\eta}$ is measurement noise, $\mathbf{o}\mathbf{x} \in \mathbb{R}^3$ is the 3D landmark on the seafloor in a global frame coordinate \mathbf{o} that is observed from this i^{th} keypoint, and r_i is the range to this landmark. $\pi(\cdot)$ is a function that transforms a 3D landmark from the global frame coordinate to the sensor frame coordinate \mathbf{s} :

$${}^s\bar{\mathbf{x}} = {}^b\mathbf{T}_s^{-1} \cdot {}^o\mathbf{T}_b^{-1} \cdot \mathbf{o}\bar{\mathbf{x}}. \quad (2)$$

Here ${}^o\mathbf{T}_b \in \text{SE}(3)$ is the AUV body pose* of current ping that contains the i^{th} keypoint, and ${}^b\mathbf{T}_s$ is sensor offset from

*we omit the subscript 'b' later to avoid ambiguity with ping index.

the AUV body to the sensor, which is normally assumed as fixed and known. Note that ${}^o\bar{\mathbf{x}} \in \mathbb{E}^3$ denotes the homogeneous representation of ${}^o\mathbf{x}$.

2) *Relative Pose Estimation*: Given a keypoint pair that observes the same 3D landmark, the landmark and relative pose can be estimated via minimizing the minus log of least squares cost, assuming the measurement noises as Gaussian:

$$\begin{aligned} \mathcal{C}({}^o\mathbf{T}_i, {}^o\mathbf{x}) &= \frac{1}{2} \left(\sum_{i=1}^2 [(\hat{\mathbf{z}}_i - \mathbf{z}_i) \Sigma_i^{-1} (\hat{\mathbf{z}}_i - \mathbf{z}_i)^\top] \right. \\ &\quad \left. + [({}^1\hat{\mathbf{T}}_2 - {}^1\mathbf{T}_2) \Sigma_t^{-1} ({}^1\hat{\mathbf{T}}_2 - {}^1\mathbf{T}_2)^\top] \right) + \phi({}^o\mathbf{T}_1), \end{aligned} \quad (3)$$

with the first term being the keypoint measurement cost discussed above, the second term the odometry measurement cost and the third term a prior cost. Specifically, ${}^1\hat{\mathbf{T}}_2 = {}^o\mathbf{T}_1^{-1} \cdot {}^o\mathbf{T}_2$ is the relative pose between pings of the keypoints, and ${}^1\mathbf{T}_2$ is the measurement obtained from dead-reckoning data. The odometry term is crucial as it helps to relieve the underconstrained issue in side-scan measurement and ensure convergence to a desired minimum. $\phi(\cdot)$ is a prior model that sets one of the poses (e.g., ${}^o\mathbf{T}_1$ here) fixed and only adjust for the other, which is reasonable as we aims to estimate the relative pose between them rather than estimate both. A factor graph describing Eq. 3 is illustrated in Fig. 4 right.

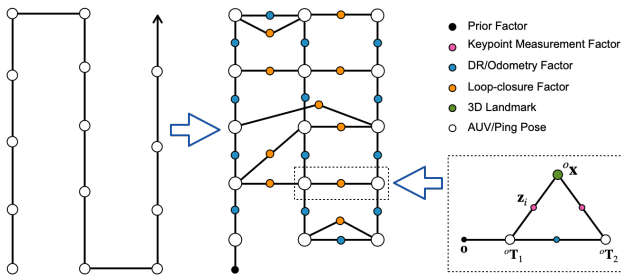


Fig. 4. Factor graph representation of our proposed SSS SLAM framework. Left: an AUV surveying trajectory. Centre: factor graph of global pose trajectory. Right: factor graph for relative pose estimation.

Σ_i is the covariance matrix for each keypoint measurement. The variance in the range measurement is dominated by the discretization of the range in the side-scan, varying from $0.01-1m^2$ depending on the resolution of the image. For the second term restricting the landmark to lie in the plane, the variance should grow as the square of the horizontal distance from the sonar. Since the sonar is mostly used at shallow grazing angles, we can instead use the range so that:

$$\Sigma_i = \begin{pmatrix} \sigma_r^2 & 0 \\ 0 & r_i^2 \alpha^2 \end{pmatrix}, \quad (4)$$

where α is the beam width in radians. The covariance matrix Σ_t is set proportional to the distance between the two dead-reckoning poses. Eq. 3 can be solved iteratively using an optimization method such as Levenberg-Marquardt algorithm, and the output relative pose is used as a loop-closing constraint for the final global optimization.

3) *Global Optimization*: We model the SLAM problem as a factor graph as demonstrated in Fig. 4 centre. The factor graph formulation is highly intuitive and allows for efficient implementation of batch [31] and incremental [32] solvers.

Two types of measurements are considered in the problem: the odometry measurements and the loop-closure measurements. The dead-reckoning system provides a smooth yet drifted AUV poses, which can be used to form odometry measurements between consecutive poses as a chain in the graph. The odometry measurement error $\mathbf{e}_n({}^o\mathbf{T}_n, {}^o\mathbf{T}_{n+1})$ is defined as:

$$\mathbf{e}_n({}^o\mathbf{T}_n, {}^o\mathbf{T}_{n+1}) = {}^o\mathbf{T}_n^{-1} \cdot {}^o\mathbf{T}_{n+1} - {}^n\mathbf{T}_{n+1}^{odo} + \boldsymbol{\eta}, \quad (5)$$

where ${}^n\mathbf{T}_{n+1}^{odo}$ is the odometry measurement obtained from dead-reckoning data. The estimated relative pose between each pair of matched keypoints is used as a loop-closure measurement ${}^i\mathbf{T}_j^{lc}$ between the corresponding i and j pings, such that the loop-closure measurement error $\mathbf{e}_m({}^o\mathbf{T}_i, {}^o\mathbf{T}_j)$ is denoted as:

$$\mathbf{e}_m({}^o\mathbf{T}_i, {}^o\mathbf{T}_j) = {}^o\mathbf{T}_i^{-1} \cdot {}^o\mathbf{T}_j - {}^i\mathbf{T}_j^{lc} + \boldsymbol{\eta}. \quad (6)$$

Given that all the measurements follow Gaussian distributions, the AUV poses can be computed by minimizing the minus log of least squares cost as:

$$\mathcal{C}({}^o\mathbf{T}_n) = \frac{1}{2} \left(\sum_{n=1}^N [\mathbf{e}_n \Sigma_n^{-1} \mathbf{e}_n^\top] + \sum_{m=1}^M [\mathbf{e}_m \Sigma_m^{-1} \mathbf{e}_m^\top] \right), \quad (7)$$

where N and M is the number of odometry and loop-closure edges in the graph, respectively. Σ_n is the odometry covariance that can be decided in a similar way as Σ_t , and Σ_m is the covariance of loop-closure measurement that comes together with the estimated relative pose. Note that we omit the constant prior factor as shown in Fig. 4 (centre) here to simplify the equation. We solve for Eq. 7 incrementally using ISAM2 [32], i.e., the whole pose graph are updated iteratively from the previous solution, when there are new measurements extracted from an input side-scan image and added to the graph. In this case we can avoid the increase of drift over a long trajectory causing the linearization to be far off that the wrong local minimal is found.

IV. EXPERIMENTS

A. Data Collection and Annotation

The SSS data tested in this work consist of 5 survey lines collected by Gothenburg University's Hugin AUV. The data was collecting approximately 4 pings per second with the AUV speed at 2m/s. The 5 survey lines following a lawnmower pattern are roughly parallel to one another and have large overlap between each other. The seafloor of the surveyed area is locally flat, with lots of trawling marks.

We manually annotate sets of keypoints between each pair of the overlapped images for evaluation purpose. The annotation process is conducted efficiently with the help of a 3D mesh of the bathymetry that is constructed from MBES data. The 3D mesh is used to find an initial guess of the potential corresponding keypoints when the annotator

identifies a keypoint in one SSS image. Thus, given the proposed correspondences, the annotator only needs to inspect and confirm the correctness of the correspondence based on the image appearance. Using this method, we obtain about 250~500 keypoint correspondences for each overlapping image pairs, see Fig. 3 right and Tab. I.

TABLE I
AMOUNT OF ANNOTATED AND DETECTED KEYPOINT CORRESPONDENCES.

Image Pair	0-1	0-2	0-3	0-4	1-2	1-3	1-4	2-3	2-4	3-4
Annotated	413	289	274	275	462	337	306	391	340	420
Detected	43	25	54	23	49	22	24	53	45	38

B. Experimental Results

In principle, a landmark observed from different ping pose should have a unique global position in ideal scenario. Based on this criteria, we propose to compute the *landmark consistency error* using annotated keypoints and the bathymetry mesh from MBES data. In particular, for each keypoint pair, we project both keypoints onto the mesh by ray-casting and find their intersections with the mesh [33], respectively. Then the Euclidean distance between both intersected landmarks is used as the error metric, i.e., the smaller this consistency error it is, the more accurate the ping poses they are. Results are shown in Fig. 5. We can see that our SLAM estimation using annotated keypoints shows consistent error reductions in all image pairs, with an average error dropping by 2.9m (63%). Similar trend of improvements can also be seen in our SLAM estimation using detected keypoints (21% overall), except for poses between image pair 2-3.

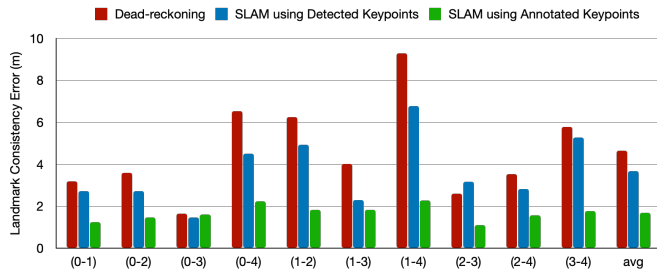


Fig. 5. Landmark consistency errors that are averaged on all the annotated keypoint correspondences between each SSS image pair and over all pairs. Note that the X axis represents the index of each image pair.

We also compute the absolute trajectory error (ATE) [34] to evaluate absolute pose consistency, by treating the estimated pose trajectory using annotated keypoints as 'ground truth' baseline. Fig. 6 demonstrates the error comparison of the whole trajectory, where our estimated trajectory has less errors at most pings, except for the ones between 4-4.3k, where the AUV turns back, and there is no detected keypoint constraint for corrections, as can be seen in Fig. 7 the zoom-in window. Overall, the estimated trajectory is closer to the 'ground truth' trajectory, with an 25% improvement over dead-reckoning in root mean squared error (RMSE), see Tab. II. Interestingly, we can notice that the trajectory error with dead-reckoning does not always grow linearly over time,

as Hugin running a lawnmower pattern could cancel out the drift growth obtained from body-fixed velocity and heading errors [35]. Similar effect can be observed in the landmark consistency error with dead-reckoning in Fig. 5.

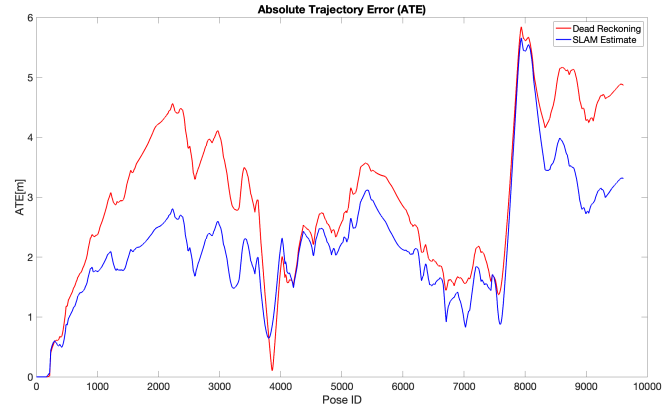


Fig. 6. Comparison of absolute trajectory error (ATE) between SLAM estimation using annotated keypoints and dead-reckoning trajectory.

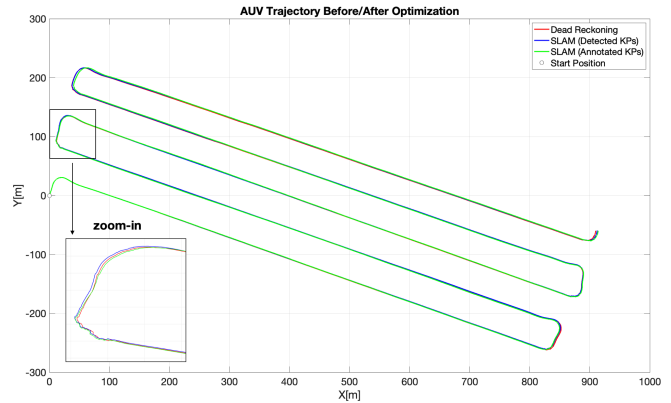


Fig. 7. Comparison of absolute trajectory error (ATE) between SLAM estimations and dead-reckoning trajectory.

TABLE II
COMPARISON OF ATE BETWEEN SLAM ESTIMATION AND DEAD-RECKONING TRAJECTORY IN ROOT MEAN SQUARED ERROR.

	Dead-reckoning	Estimated
E_{ate} (m)	3.2668	2.4414

To evaluate the quality of detected keypoint correspondences, we make use of the 3D mesh in a similar way as the landmark consistency metric. Specifically, for each pair of evaluated keypoint correspondence, we project one (e.g., from source image) onto the mesh and find the intersected landmark. Then we search in the target image for a keypoint that has the same intersected landmark on the mesh or close enough ($<0.3m$), and treat it as a baseline correspondence. We compute the end-point error (EPE) [36], i.e., the pixel distance between the detected and baseline correspondence as metric. Note that the baseline we calculate does not represent the true value, since it is searched by ray-casting using

ping poses and 3D mesh that are not absolute accurate, but we could observe the relative comparison, especially when the EPE of annotated keypoints are also added to compare, as shown in Fig. 8. We can see that our detected keypoints performs well in u (longitudinal) direction, where errors at some image pairs are pretty close to those of annotated keypoints. This indicates the sliding compatibility check in pings does help increase the matching accuracy along u direction. However, the accuracy in v (lateral) direction is much worse due to having no constraint to regularize.

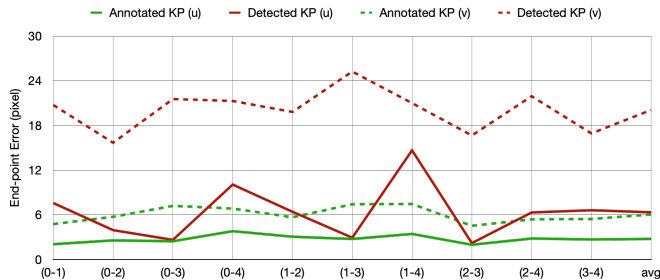


Fig. 8. Averaged end-point errors of annotated and detected keypoint correspondences between each SSS image pair and over all pairs. Here u and v denote longitudinal and lateral direction of the image, respectively.

C. Discussion

When solving Eq. 3 for relative pose and landmark, we discover a degenerate case of landmark depth ambiguity as shown in Fig. 9, where the two circles are intersected in a line segment. The solution of landmark could be either end of this line segment (i.e., ${}^o\mathbf{x}$ or ${}^o\mathbf{x}'$) under range constraints, and the converging direction is highly relevant to the initial values of the estimated landmark. We believe this ambiguity, together with measurements uncertainties, makes the solver prone to non-convergence or convergence towards an undesired minimum. Adding a prior on the landmark depth could help relieve from this issue. We thereby use geo-referenced images to initialize the x and y values of the estimated landmark. For z (depth), we use the depth of the nearer ping pose as a prior, and set its uncertainty that is proportional to the Euclidean distance between its approximated position and position of this ping pose.

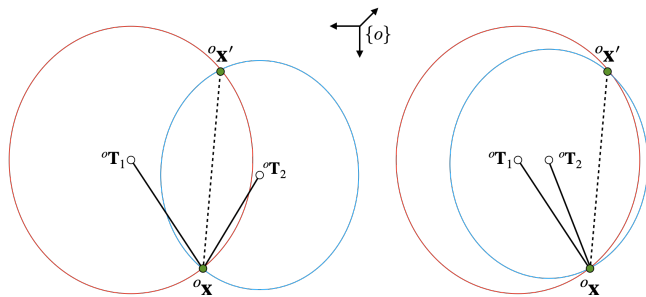


Fig. 9. Illustration of degeneracy due to landmark depth ambiguity. Left: two pings observing a landmark in between them. Right: two pings observing a landmark on the same side.

Fig. 10 shows the comparison of landmark depth estimation with and without depth prior. We can see that the

depth errors become variably large without depth prior, while adding depth prior makes the estimate more consistent and accurate. Note that this prior only works fairly well for a relatively flat seafloor with slight sloping like the tested data in this paper, but not for uneven seabed with rich hills, holes and rocks. In that case, a high precision 3D mesh from MBES could provide strong prior to reduce this depth ambiguity, but this is out of scope of this paper.

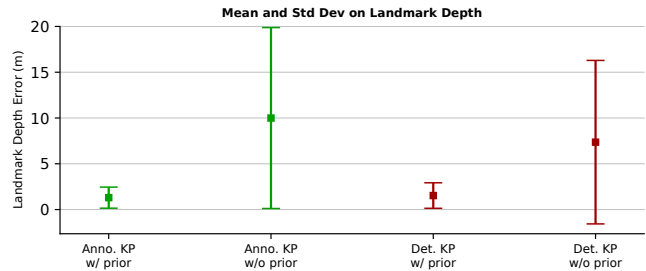


Fig. 10. Mean and standard deviation of landmark depth error with (w/) and without (w/o) depth prior over all the estimated landmarks using annotated and detected keypoints, respectively. The depth error is computed using the 3D bathymetry mesh from MBES as reference.

V. CONCLUSION

In this paper we present a feature-based SLAM framework using side-scan sonar to improve the AUV pose trajectory from dead-reckoning data. The proposed framework automatically detects keypoint correspondences between SSS images and formulates them as constraints to refine the pose trajectory through graph optimization. We carefully test and analyse our method on real data collected by Hugin AUV, and demonstrate its effectiveness. Experimental results show that the proposed method is able to effectively reduce the drift in dead-reckoning trajectory with only side-scan sensor measurements.

Though a robust keypoint matching algorithm is proposed in this paper, there is much space to improve quantitatively and qualitatively, as shown in Tab. I and Fig. 8. The main issue lies in not being able to detect rich repetitive keypoints that can be tracked across side-scan images. This could be possibly solved by data-driven methods [37] [38], which would be an interesting future direction, while to achieve that, more annotated keypoints are needed as training data.

ACKNOWLEDGMENT

This work was supported by Stiftelsen fr Strategisk Forskning (SSF) through the Swedish Maritime Robotics Centre (SMaRC) (IRC15-0046) and the Wallenberg AI, Autonomous Systems and Software Program (WASP) funded by the Knut and Alice Wallenberg Foundation.

REFERENCES

- [1] S. Thrun, "Probabilistic robotics," *Communications of the ACM*, vol. 45, no. 3, pp. 52–57, 2002.
- [2] A. Palomer, P. Ridao, and D. Ribas, "Multibeam 3d underwater slam with probabilistic registration," *Sensors*, vol. 16, no. 4, p. 560, 2016.
- [3] I. Torroba, N. Bore, and J. Folkesson, "Towards autonomous industrial-scale bathymetric surveying," in *2019 IEEE/RSJ International Conference on Intelligent Robots and Systems (IROS)*. IEEE, 2019, pp. 6377–6382.

- [4] X. Lurton, *An introduction to underwater acoustics: principles and applications*. Springer, 2002, vol. 2.
- [5] J. Aulinas, X. Lladó, J. Salvi, and Y. R. Petillot, "Feature based slam using side-scan salient objects," in *OCEANS 2010 MTS/IEEE SEATTLE*. IEEE, 2010, pp. 1–8.
- [6] J. Aulinas, A. Fazlollahi, J. Salvi, X. Lladó, Y. Petillot, J. Sawas, and R. Garcia, "Robust automatic landmark detection for underwater slam using side-scan sonar imaging," in *Proceedings of the 11th International Conference on Mobile Robots and Competitions*, 2011, pp. 21–26.
- [7] I. T. Ruiz, Y. Petillot, and D. M. Lane, "Improved auv navigation using side-scan sonar," in *Oceans 2003. Celebrating the Past... Teaming Toward the Future (IEEE Cat. No. 03CH37492)*, vol. 3. IEEE, 2003, pp. 1261–1268.
- [8] S. Reed, I. T. Ruiz, C. Capus, and Y. Petillot, "The fusion of large scale classified side-scan sonar image mosaics," *IEEE transactions on image processing*, vol. 15, no. 7, pp. 2049–2060, 2006.
- [9] M. F. Fallon, M. Kaess, H. Johannsson, and J. J. Leonard, "Efficient auv navigation fusing acoustic ranging and side-scan sonar," in *2011 IEEE International Conference on Robotics and Automation*. IEEE, 2011, pp. 2398–2405.
- [10] S. J. Julier and J. K. Uhlmann, "A counter example to the theory of simultaneous localization and map building," in *Proceedings 2001 ICRA. IEEE International Conference on Robotics and Automation (Cat. No. 01CH37164)*, vol. 4. IEEE, 2001, pp. 4238–4243.
- [11] L. Bernicola, D. Guériot, and J.-M. Le Caillec, "A hybrid registration approach combining slam and elastic matching for automatic side-scan sonar mosaic," in *2014 Oceans-St. John's*. IEEE, 2014, pp. 1–5.
- [12] M. Kaess, A. Ranganathan, and F. Dellaert, "isam: Incremental smoothing and mapping," *IEEE Transactions on Robotics*, vol. 24, no. 6, pp. 1365–1378, 2008.
- [13] M. Issartel, D. Guériot, N. Aouf, and J.-M. Le Caillec, "Robust slam for side scan sonar image mosaicking," in *OCEANS 2017-Anchorage*. IEEE, 2017, pp. 1–10.
- [14] J. Neira and J. D. Tardós, "Data association in stochastic mapping using the joint compatibility test," *IEEE Transactions on robotics and automation*, vol. 17, no. 6, pp. 890–897, 2001.
- [15] K. Siantidis, "Side scan sonar based onboard slam system for autonomous underwater vehicles," in *2016 IEEE/OES Autonomous Underwater Vehicles (AUV)*. IEEE, 2016, pp. 195–200.
- [16] M. F. Fallon, G. Papadopoulos, J. J. Leonard, and N. M. Patrikalakis, "Cooperative auv navigation using a single maneuvering surface craft," *The International Journal of Robotics Research*, vol. 29, no. 12, pp. 1461–1474, 2010.
- [17] C. M. MacKenzie, M. L. Seto, and Y. Pan, "Extracting seafloor elevations from side-scan sonar imagery for slam data association," in *2015 IEEE 28th Canadian Conference on Electrical and Computer Engineering (CCECE)*. IEEE, 2015, pp. 332–336.
- [18] J. Petrich, M. F. Brown, J. L. Pentzer, and J. P. Sustersic, "Side scan sonar based self-localization for small autonomous underwater vehicles," *Ocean Engineering*, vol. 161, pp. 221–226, 2018.
- [19] P. J. Besl and N. D. McKay, "Method for registration of 3-d shapes," in *Sensor fusion IV: control paradigms and data structures*, vol. 1611. Spie, 1992, pp. 586–606.
- [20] E. Westman, A. Hinduja, and M. Kaess, "Feature-based slam for imaging sonar with under-constrained landmarks," in *2018 IEEE International Conference on Robotics and Automation (ICRA)*. IEEE, 2018, pp. 3629–3636.
- [21] J. Li, M. Kaess, R. M. Eustice, and M. Johnson-Roberson, "Pose-graph slam using forward-looking sonar," *IEEE Robotics and Automation Letters*, vol. 3, no. 3, pp. 2330–2337, 2018.
- [22] E. Westman and M. Kaess, "Degeneracy-aware imaging sonar simultaneous localization and mapping," *IEEE Journal of Oceanic Engineering*, vol. 45, no. 4, pp. 1280–1294, 2019.
- [23] W. Xu, L. Li, Y. Xie, J. Zhang, and J. Folkesson, "Evaluation of a canonical image representation for sidescan sonar," in *2023 OCEANS-Limerick*. IEEE, 2023.
- [24] E. Coiras, Y. Petillot, and D. M. Lane, "Multiresolution 3-d reconstruction from side-scan sonar images," *IEEE Transactions on Image Processing*, vol. 16, no. 2, pp. 382–390, 2007.
- [25] A. Burguera and G. Oliver, "Intensity correction of side-scan sonar images," in *Proceedings of the 2014 IEEE Emerging Technology and Factory Automation (ETFA)*. IEEE, 2014, pp. 1–4.
- [26] M. D. Aykin and S. Negahdaripour, "Forward-look 2-d sonar image formation and 3-d reconstruction," in *2013 OCEANS-San Diego*. IEEE, 2013, pp. 1–10.
- [27] P. King, A. Vardy, P. Vandrish, and B. Anstey, "Real-time side scan image generation and registration framework for auv route following," in *2012 IEEE/OES Autonomous Underwater Vehicles (AUV)*. IEEE, 2012, pp. 1–6.
- [28] E. Rosten and T. Drummond, "Machine learning for high-speed corner detection," in *European conference on computer vision*. Springer, 2006, pp. 430–443.
- [29] D. G. Lowe, "Distinctive image features from scale-invariant keypoints," *International journal of computer vision*, vol. 60, no. 2, pp. 91–110, 2004.
- [30] M. A. Fischler and R. C. Bolles, "Random Sample Consensus: A Paradigm for Model Fitting with Applications to Image Analysis and Automated Cartography," *Communications of the ACM*, vol. 24, no. 6, pp. 381–395, 1981.
- [31] F. Dellaert and M. Kaess, "Square root sam: Simultaneous localization and mapping via square root information smoothing," *The International Journal of Robotics Research*, vol. 25, no. 12, pp. 1181–1203, 2006.
- [32] M. Kaess, H. Johannsson, R. Roberts, V. Ila, J. J. Leonard, and F. Dellaert, "isam2: Incremental smoothing and mapping using the bayes tree," *The International Journal of Robotics Research*, vol. 31, no. 2, pp. 216–235, 2012.
- [33] N. Bore and J. Folkesson, "Neural shape-from-shading for survey-scale self-consistent bathymetry from sidescan," *IEEE Journal of Oceanic Engineering*, 2022.
- [34] J. Sturm, N. Engelhard, F. Endres, W. Burgard, and D. Cremers, "A benchmark for the evaluation of rgb-d slam systems," in *2012 IEEE/RSJ international conference on intelligent robots and systems*. IEEE, 2012, pp. 573–580.
- [35] B. Jalving, K. Gade, O. K. Hagen, and K. Vestgard, "A toolbox of aiding techniques for the hugin auv integrated inertial navigation system," in *Oceans 2003. Celebrating the Past... Teaming Toward the Future (IEEE Cat. No. 03CH37492)*, vol. 2. IEEE, 2003, pp. 1146–1153.
- [36] D. Sun, S. Roth, and M. J. Black, "A quantitative analysis of current practices in optical flow estimation and the principles behind them," *International Journal of Computer Vision*, vol. 106, pp. 115–137, 2014.
- [37] P.-E. Sarlin, D. DeTone, T. Malisiewicz, and A. Rabinovich, "Superglue: Learning feature matching with graph neural networks," in *Proceedings of the IEEE/CVF conference on computer vision and pattern recognition*, 2020, pp. 4938–4947.
- [38] J. Sun, Z. Shen, Y. Wang, H. Bao, and X. Zhou, "Loftr: Detector-free local feature matching with transformers," in *Proceedings of the IEEE/CVF conference on computer vision and pattern recognition*, 2021, pp. 8922–8931.